

Evaporation Dynamics of Water Droplets on Superhydrophobic Nanograss Surfaces

Ahmed Aldhaleai^a, Faheem Khan^{b,d}, Thomas Thundat^{c,d}, Peichun Amy Tsai^{a,*}

^a*Department of Mechanical Engineering, University of Alberta, Edmonton, Alberta T6G 1H9, Canada*

^b*Fourien Inc. Edmonton, Alberta, Canada*

^c*Chemical and Biological Engineering, University of Buffalo, Buffalo, New York 14260-4200*

^d*Chemical and Materials Engineering, University of Alberta, Edmonton, AB T6G 1H9, Canada*

Abstract

Evaporation of a sessile droplet on superhydrophobic surfaces has various applications due to their utmost water-repellent and self-cleaning wetting properties. We experimentally investigate the evaporation dynamics of water droplets and the time evolution of the contact angle and drop dimensions on superhydrophobic, nanograss substrates of an extremely-low solid packing fraction ($\phi \approx 0.005$). The experimental data shows that all the droplets deposited initially form a gas-trapping, Cassie-Baxter state. Small droplets subsequently evaporate with a constant contact angle mode, followed by a mixed mode at the end of the droplet lifetime. On the contrary, for relatively large droplets, two distinct evaporation modes are found. Some of the larger evaporating droplets were initially in a constant contact angle mode and underwent a mixed mode, while others began with a mixed mode with slowly decreasing base diameter and contact angle. Intriguingly, stick-slip motions of the contact line for large droplets are observed using superhydrophobic nanograss surfaces. Such slip or jumping motion could be related to the excess free energy available in the system when the receding contact angle is reached, resulting in the contact line movement. Finally, the experimental data of contact angle dependent evaporative mass flux are found to nearly collapse onto one universal curve for different droplet sizes and initial contact angles, in agreement with an evaporative cooling model.

Keywords: Evaporation dynamics, Nanograss, Superhydrophobic surfaces, Stick-slip motion, Contact angle, Cassie-Baxter state

1. Introduction

Droplet evaporation is an omnipresent process that also finds plentiful decisive applications, including watercolor painting [1], droplet-based microfluidics [2], DNA extraction [3], inkjet printing [4, 5, 6], and fabrications of bio-materials and photonic crystals through self-assembly [6, 7, 8]. Therefore, fundamental understanding of droplet evaporation dynamics under various key parameters, such as surface structure or roughness [9, 10], nano-particle suspensions [11, 12], and surface wettability [13] is crucial so as to control the processes tailored for the desired applications. In particular, evaporating droplets on superhydrophobic (SH) surfaces has recently received a significant interest because of their promising applications for self-cleaning [14, 15, 16], improving corrosion resistance [17], optical devices

[18, 19, 20], anti-icing [21, 22], anti-fouling [23], friction control [24], and drag reduction [25, 26, 27, 24]. In addition to drop evaporation, the wettability effect also has a key influence on dropwise condensation [28] and boiling heat transfer characteristics [29, 30, 31].

SH surfaces are commonly characterized by a large contact angle ($\theta \gtrsim 150^\circ$) with water and small contact angle hysteresis (CAH), the difference between advancing and receding contact angles [32]. Deposition of water droplets on SH surfaces relies on the interplay between surface chemistry and roughness, while two common wetting modes are observed: (i) Cassie-Baxter wetting (CB or the so-called “Fakir”) with air (or vapor) trapped underneath the droplet [32, 33, 34] and (ii) Wenzel (W) regime where the liquid fills in the surface cavities [35]. Albeit various beneficial applications, it has remained challenging to use superhydrophobic surfaces for long-term stability since most of them lose their liquid-repellency once exposed to

*Corresponding author: peichun.amy.tsai@ualberta.ca

chemical [36], surfactant additives [37, 38, 39] or high temperature environments [40, 41]. Another factor that limits the commercialize use of the SH surfaces is the occurrence of the irreversible wetting transition from Cassie-Baxter to Wenzel state during evaporation [10, 32, 42, 43, 44, 45, 46, 47], thereby destroying the superhydrophobicity of a low CAH and air-trapping state.

Both static wetting (in terms of static contact angle) and water evaporation dynamics on SH micro-textures, e.g., regular micro-pillars [3, 10, 46, 48, 49, 50, 51, 52, 53], random micro-fibers [15, 36, 40], or micrometer-sized mushroom-shaped pillars [54, 55], have been actively studied over the last two decades. Whereas, in comparison, fewer studies have been conducted on SH nano-scale structures or fibers [9, 10, 14, 17, 18, 22, 40, 37, 56] primarily due to challenges of nano-fabrications. In addition to the packing fraction, ϕ , the length scale of surface roughness can play a crucial role in the pinning (or retention) and de-pinning forces exerted on droplets by solid surfaces/textures [53], thereby affecting contact line movement and evaporation modes of water droplets on various SH surfaces. The evaporation dynamics and dynamic wetting on superhydrophobic nano-textured surfaces (e.g., SH nanoglass-like surfaces), however, have been investigated to a less extent [57, 58, 59, 60, 61]. In particular, experiments regarding the contact line movement of evaporating drops on SH nanoglass surfaces (with pointy or needle-like contact areas) are rare, and the full understanding is still missing. Further investigations are hence needed to shed light on the roughness effect on evaporation modes and rates as well as contact line movement on various SH surfaces.

In this work, we fabricated SH nanoglass-like surfaces and investigated the initial wetting state, evaporating dynamics, and contact line movement of a naturally-evaporating water droplet on such SH surfaces of random nano-scale roughness, with an extremely low solid packing fraction, $\phi = 0.005 \pm 0.003$, and surface roughness, $r = 1.05 \pm 0.01$ (see Fig. 1). Here, ϕ and r are conventionally defined as the ratio of the liquid-solid surface area to the total (liquid-solid and liquid-gas) areas and the ratio of the total surface area to the projected one (on a 2D plane), respectively, and estimated using a nanocone geometry (see Supplementary Information, SI, for details). Systematic measurements of the droplet contact angle, base diameter, height, and volume were performed for several SH nanoglass surfaces. Our results highlight the influences of nano-roughness and droplet size on the evaporation dynamics. By increasing the droplet size, for the first time, stick-slip motions

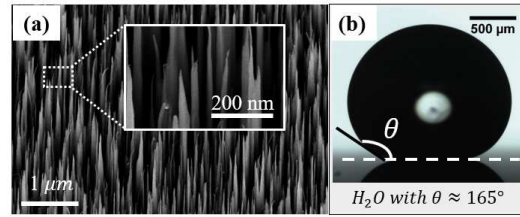


Figure 1: (a) SEM image of superhydrophobic nanoglass (NG) surface with spiky nanoscale structure; (b) the corresponding side-view snapshot showing a large contact angle ($\theta \approx 165^\circ$) of a water droplet.

of the contact line for large droplets on SH nanoglass surfaces of low ϕ were studied.

2. Experimental

2.1. Sample Preparation

Several SH nanoglass surfaces were fabricated using reactive ion etching (RIE) on 4-inch wafers, cleaned using a standard piranha solution in prior. Fig. 1a shows side-view, SEM image of such SH surface used. The formation of nanoglass is a result of the passivation and etching process in a standard RIE etching process. The RIE etching is performed using a mixture of H_2 and O_2 gases with a flow rate of 100 standard cubic centimeters per minute (sccm) and 80 sccm, respectively. Additionally, trace value of SF₆ plasma is also supplied and used during the etching process. The etching and passivation steps are performed at a pressure of 80 mTorr and 150 mTorr, respectively. During RIE, plasma power is adjusted between 150W and 135W for the steps of passivation (for 52 s) and etching (for 12 s), respectively. After the nanoglass formation, the wafer is coated with photoresist, which provided protection during the subsequent step of dicing. After dicing, each 1 cm × 1 cm piece is soaked in acetone overnight; this step helps in removing photoresist completely. With this fabrication method, the nanoglass pillars are formed with various heights. Close to the edge of a substrate, the height could dramatically reduce by $\approx 50\%$. The surface hydrophobicity is caused by the passivation of a mixture of the gases H₂/O₂/SF₆ and the high density of the spikes.

2.2. Droplet Evaporation Experiments

For the evaporation experiments, water droplets of 8-12-μL are gently deposited on the NG surface using a syringe pump. One camera (Thorlabs DCC3240C) coupled with a long-range magnifying lens (Navitar 12×) was used to record side-view of the evaporating droplet

at 1 fps (frame per second). Fig. 1b is such a snapshot showing the initial wetting state of Cassie-Baxter state [32], while air is trapped beneath, and the drop rests on the top of the nanograss with a large contact angle, $\theta > 160^\circ$.

To analyze the evaporation dynamics, we first extracted the shape of droplets from the side-view snapshots using ImageJ software [62]. Subsequently, a custom Matlab code based on the axisymmetric drop shape analysis (ADSA) method was applied to measure the drop volume (V), contact angle (θ), droplet height (h), and the drop size (in terms of the contact diameter, D_b). The ADSA method numerically fits a theoretical Laplacian curve based on the Young–Laplace equation with the gravitational effect with known surface tension values to an experimental profile of the drop shape obtained [63, 64, 65]. The experiments were performed under ambient temperature ($22 \pm 1^\circ\text{C}$) at 1 atm and slightly varying relative humidity (RH) conditions. The reproducibility of the results was checked by repeating 4-5 independent experiments on the SH NS surfaces, and we report the standard deviations as the errors for θ , D_0 , and D_b .

3. Results and Discussion

3.1. Evaporation Dynamics

Fig. 2 illustrates the evaporation dynamics of water droplets on SH nanograss (NG) surface in terms of dimensionless time (t/t_f) normalized by the total evaporation time (t_f), under slightly different RH $\approx 24.8 \pm 1.2\%$. Fig. 2 shows that the droplet on the SH NG surfaces began with a large $\theta \approx 166^\circ \pm 1.5^\circ$ in a CCA mode, in agreement with a CCA-mode evaporation observed on SH surfaces with nano-roughness and a low CAH $\approx 5^\circ$ by Kulinich et al. [67]. In comparison, previous data of the evaporation dynamics on SH nano-structured (NS) pillars [10] started with a CCR mode, subsequently followed by a CCA mode, and ended the evaporation with a mixed mode. Remarkably, all the water droplets on SH NG surfaces were initially in a CB state, whereas the droplets on SH nanostructured pillars can form a CB droplet for high roughness $r > 3.51$ and a Wenzel droplet for relatively low $r < 1.98$ [10], as shown in Fig. 2 a-b.

As revealed in Fig. 2b, for SH nanograss surfaces we observed that for small water droplets (of initial diameter $D_0 \approx 2.6 \pm 0.17$ mm) the contact diameter (D_b) decreases linearly with the dimensionless time from 0 to 90% t_f at a slope of $\approx -1 \pm 0.2$, implying a very mobile contact line without pinning on SH NG surfaces. This

corresponds to the linearly decreasing of D_b/D_0 with a decaying slope of $\beta = -0.39 \pm 0.04$, obtained with a best linear-fit in Fig. 2b, because of simultaneous decreasing H and V during evaporation (shown in Fig. 2c and Fig. 2d, respectively).

Fig. 2d reveals that the droplet volume changes non-linearly with time, consistent with the evaporation characteristics on SH carbon nanofibers (CNF) [66] with a random structure and large initial $\theta \approx 150^\circ$. However, the evaporation mode observed on such SH CNFs of random roughness is CCR [66], different from the CCA initially observed by our SH Nanograss surface. In comparison, recent studies on SH nanoporous membrane made of hydrophobized anodic aluminium oxide (AAO) show a CCR mode of evaporating droplets, with a pinned contact line, during most of evaporation time [68]. The authors discussed that evaporating water droplets stick on such surfaces, very likely, because of air entrapped in the nanoscale pores that are not interconnecting [68]. These comparisons highlight that both ϕ and the shape or morphology of nano-textures or nano-roughness play an important role in the pinning of the contact line and, hence, initial evaporation mode, being CCR or CCA.

Once the evaporation time reaches $0.9t_f$, the transition from partially-wetting CB to Wenzel state occurs at a critical contact angle, ranging from 114° to 155.6° and critical base diameter, $D_b = 450 \pm 60 \mu\text{m}$, where the contact diameter underwent a slight increase shown by the Fig. 2b inset. We estimated that the Laplace pressure inside the droplet increased during the process from its initial value, $\Delta P_L = 111.4 \pm 6.8$ Pa to the critical Laplace pressure, ΔP_L^* , ranging from 305.4 Pa to 591.4 Pa (estimated from four independent experiments). The value of Laplace pressure is calculated using the drop radius of curvature (see SI for the details). Such CB to W transition could be triggered by the decrease in the droplet size so that the Laplace pressure increase inside the droplet from its initial value to the critical Laplace pressure. We identified such CB-W transition by an increase in D_b since water penetrates into nano-rough structures and thus enlarges the contact diameter. This method agrees with and is also used by a recent study on drops evaporating on pillar-like microtextured SH surfaces [47]. The corresponding critical contact angles, contact diameters, and Laplace pressure are reported in SI.

Water droplets on our SH NG surfaces were in a CB state with a large CA ($\theta > 160^\circ$) and evaporated mostly in CCA mode, followed by a mixed mode. During final evaporation $t > 0.9 t_f$, both θ and D_b decrease simultaneously, in a so-called mixed mode, until com-

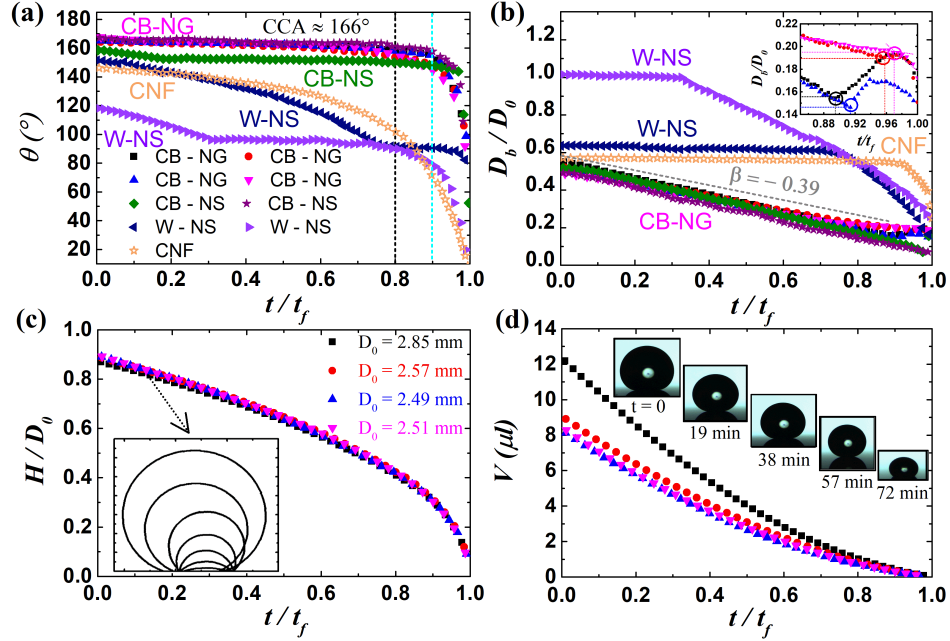


Figure 2: (Supporting movie) Time-evolution of (a) contact angle, θ , (b) dimensionless base diameter, D_b/D_0 of evaporating water droplets on the SH nanoglass (NG) surfaces (shown in Fig. 1a) (■, ●, ▲, ▼). Here, time, t , is normalized with the total evaporation time, t_f . The length scale is normalized with, D_0 , the free drop diameter of the same initial volume. Initially, for $t/t_f = 0 - 0.8$, the drop evaporates with a constant contact angle (CCA) mode with average $\theta \approx 166^\circ$, while the dimensionless contact diameter, D_b/D_0 , decreases linearly with dimensionless time with a decaying slope of $\beta = -0.39$. At the end of the evaporation (for t/t_f between 0.8 and 1), both D_b and θ decrease, corresponding to a mixed mode. The inset in (b) reveals a slight increase in D_b after $\approx 0.9t_f$ as the droplet underwent a CB to Wenzel (W) transition while water impregnating into the rough cavities. For a comparison, the previous experimental data by Bussionnière et al. [10] using more regular, nanostructures (NS) (◆, ★, ▲, ▼) and by Gelderblom et al. [66] (✱) using SH carbon nanofiber (CNF) are also plotted for θ and D_b in (a) and (b), respectively. Depicted in (c) is the dimensionless droplets, H/D_0 , for four independent droplets. The inset shows the contours for an evaporating droplet with $D_0 = 2.85$ mm. Time-varying droplet volume, V , is shown in (d), and the insets show the time evolution of droplet shape for $V_0 = 12 \mu\text{l}$.

pletely dry out [46]. Based on these observations, our SH NS surfaces revealed resilient superhydrophobicity with a later-time CB-W wetting transition after 90% of the total evaporation time, whereas, in comparison, the SH NS and the SH CNF surfaces wetted in a Wenzel mode lost their superhydrophobicity earlier with an initial contact angle $\theta < 150^\circ$ and with a pinned contact line for the most of evaporation period (see Fig. 2b).

Several different or combined evaporating modes, namely CCA, CCR, and mixed, have been observed for drop evaporation on various surfaces [10, 46, 55, 69, 70, 71, 72]. In general, the CCA mode normally happens for CB evaporating drops, since the free movement of the contact line during evaporation is maintained, while the contact angle remains constant with a gradual decrease of the contact radius [46, 48]. In contrast, a CCR mode likely occurs for a Wenzel evaporating droplet, as the strongly pinned contact line during evaporation

causes a gradual decrease in contact angle on the solid surface, while maintaining a nearly constant contact radius [71, 73]. Finally, incremental reductions in both the contact radius and contact angle can lead to a mixed mode of evaporation [48, 73]. A mixed-mode has been observed experimentally towards the end of droplet lifetime, qualitatively attributed to contact-line pinning at local heterogeneities [74, 75] or Marangoni effect [76], and quantitatively modeled with a dynamical roughness change arising due to atmospheric contamination additions [72].

From existing experimental findings using various SH surfaces, on the one hand, a CCA mode followed by a final mixed mode on SH surfaces with a small CAH has been observed during evaporation on SH surfaces of low CAH $\lesssim 5^\circ$ (e.g., with polished aluminium plates of random nano-roughness [67], with micro-pillars [48], and with lotus-leaf-like structures [77]) as well as on

micro-pillared SH surfaces with a low packing fraction (e.g., $\phi = 0.01$ [46] and $\phi = 0.042$ [47]). In contrast, three sequential stages of evaporation dynamics of (i) CCR, (ii) CCA, and (iii) mixed mode (of CCR and CCA) have been reported for SH nano- or micro-structured surfaces with a higher ϕ (e.g., nanostructured pillars with ϕ from 0.01 to 0.2 and with r between 1.16 and 4.92 [10], micro-pillars with $\phi > 0.03$ [46], mushroom-like structures with ϕ ranging from 0.19 to 0.48 [55], and microstructured SH surfaces with high CAH $\approx 95^\circ - 113^\circ$ [71]).

Combining with our data on SH NG surfaces, the above comparisons between the various experimental data reveal that, despite different types of surface morphology, water droplets on various superhydrophobic surfaces of small packing fraction ϕ and a low CAH evaporate in a CCA mode initially. On the other hand, regardless of micro or nano-sized roughness, droplets evaporate in a CCR mode initially on SH surfaces with a large CAH.

In so far, most experiments concerning SH surfaces have been conducted at an ambient condition. Only a few pioneering studies have investigated the longevity of the superhydrophobicity with exposure to substrate heating (e.g., a switchable SH surface made by a plasma spraying technology [78], SH mushroom-like pillars with the substrate temperature between 30 and 80 °C [55], and a special SH coating when a catalyst mesh used was maintained at 900 °C [79]). In addition, recent studies have shown that the superhydrophobic surfaces can improve the boiling and condensation processes and enhance the heat transfer rates due to their small solid-liquid contact area [28, 29, 30, 31]. Our SH-NG surfaces, due to their water-repellent properties and gas-trapped wetting state, are expected to influence the heat transfer rates during the boiling or condensation process, which will be of use and interest for future systematic studies. Hence, it will be intriguing to systematically investigate the influence of substrate heating on both static contact angle and evaporating modes of water droplet on SH NS surfaces with an extremely low ϕ and a delayed CB to W transition, compared to most of SH surfaces explored.

3.2. Stick-Slip motion for large droplets

In contrast to smoothly decreasing in D_b for the small droplets (of $D_0 \approx 2.6$ mm) shown in Fig. 2, stick-slip motions of the contact line were observed during the evaporation of relatively large droplets (of $D_0 \approx 4.2 \pm 0.2$ mm) deposited carefully. Fig. 3.2 a-b shows such (jumping) results of the contact angle and diameter evolution of large evaporating droplets on SH NG

surfaces, for initial air-trapping CB state for different droplets with different RH between 21% and 52%.

The above distinct behavior of the contact line movement during evaporation observed for the small and large droplets on our SH NG surfaces may be attributed to the dominant effect of droplet gravity for the large droplets. One can use the capillary length, $l_c = \sqrt{\gamma/(\rho g)}$, to compare the effect of surface tension with gravity and to characterize which effect is dominant for a small and large droplet. Here, γ is the surface tension, ρ is the liquid density, and g is the gravitational acceleration. For a water droplet at the ambient conditions ($\gamma = 72 \text{ mN/m}$), the corresponding capillary length is $l_c \approx 2.7$ mm. On the one hand, our small droplets have an average free drop radius of $R_0 = 1.3$ mm, which gives rise to $R_0/l_c \approx 0.5$, indicating dominant effect of surface tension. On the other hand, the average free drop radius for the large droplets used is about $R_0 = 2.1$ mm, which yields a comparable $R_0/l_c \approx 0.8$, implying a comparable influence between the gravity and surface tension effect. The latter situation of a comparable hydraulic pressure and Laplace pressure due to surface tension may cause the large droplets to sink deeper between the nanograss structures and hence sometimes “sticks” on the SH NS surface until the evaporating droplet has sufficient access surface energy (when sufficiently overcoming the adhesion force) to “jump” to a lower-energy state towards the equilibrium.

In addition, two distinct initial modes of evaporation were observed when depositing large water droplets $D_0 \geq 4$ mm on SH NG surfaces. First set of data (■, ◀) in Fig. 3.2 a have slightly different free drop diameter $D_0 \approx 4.04$ and 4.43 mm, respectively, and started initially at CCA mode similar to small droplets, while D_b recedes steeply. On the other hand, the other data for $D_0 \approx 4.13$ mm (●) and 4.08 mm (▲) underwent a mixed mode (of CCR and CCA) evaporation with very slowly decreasing D_b and θ . When t/t_f between 0.9 and 1, mixed mode occurs, while both θ and D_b diminishes simultaneously.

We experimentally observe that water drop has a certain initial contact angle, θ_0 , after the deposition of the droplet. Water droplet starts to lose liquid during evaporation, resulting in a deviation from that of the initial equilibrium state due to the changes in droplet shape and CA, causing the triple line to move [80]. When θ_0 reaches a minimum possible value below or equal the receding contact angle, $\theta_r \approx 156.9^\circ \pm 1.2^\circ$, which is measured by using a sessile drop method while reducing the droplet volume on the surface. Subsequently, the contact line starts to move, and the first jump is observed. The advancing contact angle for the SH NG surfaces is

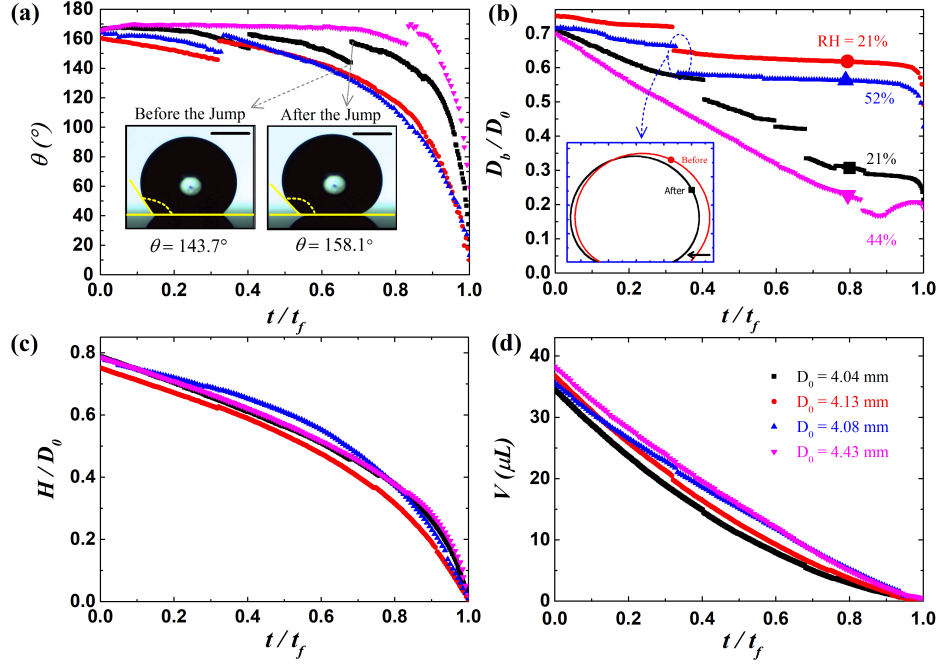


Figure 3: (Supporting movie) (a) Contact angle, θ , and (b) the normalized contact diameter, D_b/D_0 , as a function of the normalized time, t/t_f , measured for water droplets of $D_0 \approx 4.2$ mm at various relative humidity (RH). In (a) and (b), stick-slip motions are observed for large droplets, and the insets show the droplet shape before and after the jump in changing θ . The scale bar corresponds to $500 \mu\text{m}$. This trend repeated for the all stick-slip/jump events observed for various large droplets of $D_0 = 4.04$ (■), 4.13 (●), 4.08 (▲), and 4.43 (▼) mm. Depicted in (c) is the dimensionless droplet height, H/D_0 , for four independent droplets. Time-varying droplet volume, V , is shown in (d).

also measured, $\theta_a \approx 164.5^\circ \pm 0.6^\circ$, with the sessile drop method by slowly increasing the droplet volume.

With the average θ_a and θ_r measured, one can estimate the magnitude of the adhesion force, F_{adh}^0 , between the water droplet and a smooth surface, via $F_{adh}^0 = C_g R_b \gamma (\cos \theta_r - \cos \theta_a)$ [81, 82], where C_g is a geometric prefactor depending on the shape of the drop base on the solid surface ($C_g = 4/\pi$ for a circular contact, e.g., Eq. (10) in Ref. [81]), and R_b is the base radius of the droplet. For a rough substrate, the effect of packing fraction, ϕ , which could characterizes the fraction of area that the contact line can be pinned, should be considered. Hence, the corresponding adhesion force for a rough surface is modeled via [83]

$$F_{adh} = \phi C_g R_b \gamma (\cos \theta_r - \cos \theta_a). \quad (1)$$

For our rough SH NG surfaces with $\phi = 0.005$, using the above equation, the droplet adhesion forces on the SH NG surfaces are estimated to be $F_{adh} \approx 1.37 \times 10^{-8}$ and $3 \times 10^{-8} N$ for the small and large water droplets used, respectively. The order of magnitude of these adhesion

forces calculated is consistent with (but smaller than) previous estimations using micro-pillared SH surfaces [84].

The stick-slip motion is revealed by a sudden decrease of D_b and an abrupt increase in θ , indicated by the sudden movement of the three-phase contact line occurring for all the large droplets. Fig. 3.2a insets, for example, display a water droplet of $D_0 = 4.43$ mm before and after the slip or jump motion, with their θ changing from 156° to 168° (which recovers to nearly its initial value of $\theta_0 \pm 3^\circ$) and D_b from 0.96 mm to 0.82 mm.

This jumping motion is very likely attributed to the excess free energy available due to the reduction in the droplet size and θ [85]. Using the thermodynamic Gibbs free energy of the drop due entirely to interfacial free energies, Shanahan [80] proposed a theoretical model estimating certain excess energy as a criterion for contact line movement. The excess free energy per unit length is associated with the contact line movement by δr , resulting in the change in θ on smooth or rough surfaces,

and can be expressed as [80]:

$$\delta\tilde{G} \approx \frac{\gamma \sin^2 \theta_0 (2 + \cos \theta_0) (\delta r)^2}{2r}, \quad (2)$$

where γ is the surface tension at the liquid-air interface, θ_0 is the initial contact angle of the surface (i.e., the CB contact angle for our SH NG), δr is the slipped distance local to the stick-slip event, and r is local pinned contact radius before the triple line slips. Recently, Shanahan and co-workers [86] have provided an equivalent expression of the excess free energy necessary to overcome the pinning of the contact line on hydrophilic and hydrophobic substrates (and in the presence of nanoparticles) due to the change in the contact angle ($\delta\theta$). The detailed express is given in the SI.

As evaporation proceeds, the slipped distance, δr , the distance between the actual contact radius, r , and the corresponding equilibrium value, r_o , increases, and hence $\delta\tilde{G}$ increases with $(\delta r)^2$, following Eq. (2). When $\delta\tilde{G}$ reaches the potential energy barrier value, sufficient energy is available, causing the triple line to jump to its new equilibrium position at a lower contact radius. While CA after the jump recovers nearly to the initial CB CA (θ_0), as shown in Fig. 3.2a.

To calculate the excess free energy, we measured θ_0 (i.e., the initial CB contact angle for our SH NG), δr , and r during each slip events using Eq. (2) (see SI for the values). The average jumping distance, δr , on our SH NG surfaces is $132 \pm 40 \mu\text{m}$, contrastingly compared to that of approximately the micro-pillar spacing of $O(10 \mu\text{m})$ observed for evaporating droplets stick and slip on SH regular micro-pillars [51, 48]. Intriguingly, the latter indicates that the origin of the stick-slip motion of contact line stems from the pinning and de-pinning forces exerted by the individual (regular) pillars where water droplet sticks upon, which is consistent with the results reported for periodic nano-pillars by Molecular Dynamics (MD) simulation [53]. In contrast, for our SH NG surfaces due to needle-like structures, large water droplets can slip with a much greater δr due to a comparatively smaller ϕ .

The average value of $\delta\tilde{G}$ with the δr calculated for the large droplets on SH NG surfaces is about 10^{-8} J m^{-1} . This value is one order of magnitude less than that reported by Shanahan and Sefiane, i.e., in the order of magnitude of 10^{-7} J m^{-1} on randomly hydrophobic rough PTFE (Teflon) substrates [86, 87], and in the same order of magnitude of those reported by Ramos on microstructured PTFE surfaces (of $\phi \approx 0.15$) [88]. The low values of $\delta\tilde{G}$ on the microstructured PTFE and our SH NG surfaces can be attributed to a smaller ϕ for pinning and, due to less pinning and low adhesion, may

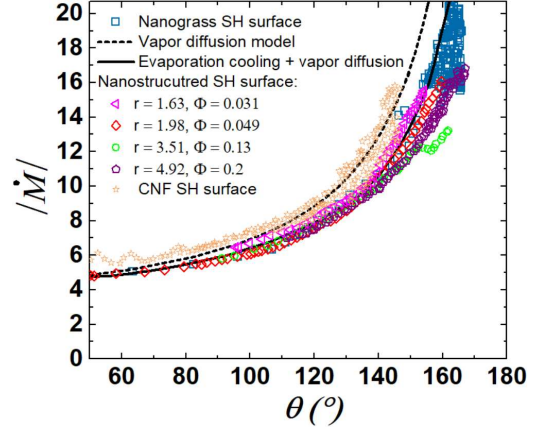


Figure 4: Water evaporation rate on SH nanograss surface. The dimensionless evaporation mass flux rate, $|\dot{M}|$ (measured from the measured droplet volume) as a function of CA (θ) for different droplets. Comparison between our experimental results (\square) with a vapor diffusion model derived by Popov [89] (\cdots) and an evaporation cooling model [95] (—) displayed that the low evaporation rate observed can be attributed to a cooling effect. For a comparison, the previous experimental data by Bussonnière et al. [10], ($\triangle, \diamond, \circ$) using SH NS and Gelderblom et al. [66], (\star) using SH carbon nanofiber (CNF) are also plotted.

contribute to more mobile contact line and hence resilient superhydrophobicity of their and our substrates. The estimated $\delta\tilde{G}$ value for our SH NS surfaces is of the same order of magnitude of that of the adhesion force F_{adh} that is estimated based on CAH using Eq. (1), implying that once the excess energy is sufficiently large to overcome the adhesion force, the drop starts to move or jump.

3.3. Evaporation Rate

A classical theory of the vapor-diffusion model is widely used to predict the evaporation mass flux across the vapor-liquid interface of an evaporating droplet [89]. This model was able to predict the evaporation rate for some experimental studies conducted in ambient air on carbon nanofiber (CNF) [66], smooth hydrophobized silicon wafers, and rough hydrophobic Teflon [90]. The simplification ingrained in the model such as assuming that vapor-diffusion is the only transport mechanism governing the droplet evaporation without considering the evaporative cooling may limit its applications to other experimental data, and it has been shown to either underpredict [91, 92] or overpredict [93, 94, 95] the evaporation rate.

Here, we compare the experimental dimensionless mass flux rate, $\dot{M} = \frac{\dot{m}}{R_b D (C_s - C_\infty)}$, in Fig. 4 using water

droplets on SH NG surface, where R_b is the base radius, D is the water vapor diffusion coefficient in air, c_s is the saturated vapor concentration, and c_∞ is the vapor concentration far away from the droplet, with the analytical vapor-diffusion model (dashed line) [89] and with a numerical simulation (solid line) considering cooling effect [95]. The direct form of the Popov model concludes that the rate of (dimensionless) mass loss only depends on the contact angle but slightly overestimates the evaporation rates measured on our SH NG surfaces.

Our data is in agreement with the recent studies by Bussonnière et al. [10] and Dash et al. [49], revealing that droplets evaporate more slowly on SH nano-patterned surfaces. Further numerical simulation [95] suggested that this deviation is likely attributed to the evaporative cooling effect. At a high contact angle, the contact diameter becomes small, limiting the heat flux between the substrate and drop, which in turn leads to a decrease of saturated vapor concentration, and hence slower evaporation. Our data reveal a better agreement with the numerical simulation considering a cooling effect during evaporation [95], and with the results using SH nano-structured surfaces [10]. At high CA, $\gtrsim 150^\circ$, the experimental data deviate from the cooling model (Solid line in Fig. 4) with a lower rate. This deviation may attribute to the spherical droplet assumption used in both models and the observed perversion of the drop shape at such a high CA from a spherical cap [89, 95].

4. Conclusions

In summary, the wetting state, evaporation dynamics, and contact line movement of evaporating water droplets on SH nanoglass surfaces with an extremely low $\phi \approx 0.5\%$ were experimentally elucidated. Different from that evaporating drops can form either CB or Wenzel state, depending on r and ϕ , on more regular SH micro- or nano-structured pillars, all small droplets on SH NG surfaces formed a gas-trapping CB wetting state and evaporated in a constant contact angle (CCA) mode for most of the droplet lifetime. Besides, beneficial to various applications, the SH nanoglass surfaces delay the CB to Wenzel Wetting transition to a later time at $0.9t_f$. In contrast to smaller drops, stick-slip motions of the contact line were observed for the first time on SH nanoglass surfaces, for large droplets of initial drop size of $D_0 \approx 4.2$ mm. This jumping motion is attributed to the excess free energy (of $O(10^{-8} \text{ Jm}^{-1})$) available in the system, due to the change in the droplet shape and contact angle, and hence the contact line movement when θ reaches θ_r . Finally, the classical vapor-diffusion model slightly overpredicts the water

evaporation rate on SH nanoglass surfaces with a low CAH and smaller contact area, while the evaporative cooling effect could better predict the evaporation rate. In terms of applications, using the superhydrophobic nanoglass surfaces water droplets evaporate mostly in a constant-contact-angle mode, with a very mobile contact line, and delay the CB to W wetting transition (to $0.9 t_f$), compared to the initial CCR mode and pinning contact line observed on most of SH regular micro-structures and nano-pillars. This suggests robust SH surfaces composed of nano-grass structures of a low ϕ ($\lesssim 0.005$) and a low CAH for advantageous, self-cleaning surfaces with water droplets.

Acknowledgement A.A. and P.A.T. thankfully acknowledge the funding support from the Natural Sciences and Engineering Research Council of Canada (NSERC) and Alberta Innovates (AI). P.A.T. holds a Canada Research Chair in Fluids and Interfaces.

Supporting Information See the supplementary document for additional SEM images, the calculations of surface parameters (ϕ and r), data of critical θ and D_b at the CB to Wenzel wetting transition, the calculations of excess energy, δG , for the stick-slip motion observed and evaporative flux, $|\dot{M}|$, and description of two videos of evaporating droplets on the SH nanoglass surfaces.

References

- [1] R. D. Deegan, O. Bakajin, T. F. Dupont, G. Huber, S. R. Nagel, T. A. Witten, Contact line deposits in an evaporating drop, *Phys. Rev. E* 62 (1) (2000) 756.
- [2] S. T. Chang, O. D. Velev, Evaporation-induced particle microseparations inside droplets floating on a chip, *Langmuir* 22 (4) (2006) 1459–1468.
- [3] G. Ciasca, L. Businaro, M. Papi, A. Notargiacomo, M. Chiarpotto, A. De Ninno, V. Palmieri, S. Carta, E. Giovine, A. Gerardino, M. De Spirito, Self-assembling of large ordered dna arrays using superhydrophobic patterned surfaces, *Nanotechnology* 24 (49) (2013) 495302.
- [4] P. Calvert, Inkjet printing for materials and devices, *Chem. Mater.* 13 (10) (2001) 3299–3305.
- [5] J. Lim, W. Lee, D. Kwak, K. Cho, Evaporation-induced self-organization of inkjet-printed organic semiconductors on surface-modified dielectrics for high-performance organic transistors, *Langmuir* 25 (9) (2009) 5404–5410.
- [6] E. Sowade, T. Blaudeck, R. R. Baumann, Self-assembly of spherical colloidal photonic crystals inside inkjet-printed droplets, *Cryst. Growth Des.* 16 (2) (2016) 1017–1026.
- [7] A. Syed, L. Mangano, P. Mao, J. Han, Y.-A. Song, Creating sub-50 nm nanofluidic junctions in a pdms microchip via self-assembly process of colloidal silica beads for electrokinetic concentration of biomolecules, *Lab Chip* 14 (23) (2014) 4455–4460.
- [8] Y. Zhao, L. Shang, Y. Cheng, Z. Gu, Spherical colloidal photonic crystals, *Acc. Chem. Res.* 47 (12) (2014) 3632–3642.

- [9] M. Ojha, A. Chatterjee, F. Mont, E. Schubert, P. C. Wayner Jr, J. L. Plawsky, The role of solid surface structure on dropwise phase change processes, *Int. J. Heat Mass Transf.* 53 (5-6) (2010) 910–922.
- [10] A. Bussonnière, M. B. Bigdeli, D.-Y. Chueh, Q. Liu, P. Chen, P. A. Tsai, Universal wetting transition of an evaporating water droplet on hydrophobic micro-and nano-structures, *Soft matter* 13 (5) (2017) 978–984.
- [11] T. A. Nguyen, M. A. Hampton, A. V. Nguyen, Evaporation of nanoparticle droplets on smooth hydrophobic surfaces: the inner coffee ring deposits, *J. Phys. Chem. C* 117 (9) (2013) 4707–4716.
- [12] M. B. Bigdeli, P. A. Tsai, Making photonic crystals via evaporation of nanoparticle-laden droplets on superhydrophobic microstructures, *Langmuir* 36 (17) (2020) 4835–4841.
- [13] G. Li, S. M. Flores, C. Vavilala, M. Schmittl, K. Graf, Evaporation dynamics of microdroplets on self-assembled monolayers of dialkyl disulfides, *Langmuir* 25 (23) (2009) 13438–13447.
- [14] Y. Lai, Y. Tang, J. Gong, D. Gong, L. Chi, C. Lin, Z. Chen, Transparent superhydrophobic/superhydrophilic tio 2-based coatings for self-cleaning and anti-fogging, *J. Mater. Chem.* 22 (15) (2012) 7420–7426.
- [15] S. Kulinich, S. Farhadi, K. Nose, X. Du, Superhydrophobic surfaces: are they really ice-repellent?, *Langmuir* 27 (1) (2010) 25–29.
- [16] J. Drelich, E. Chibowski, D. D. Meng, K. Terpilowski, Hydrophilic and superhydrophilic surfaces and materials, *Soft Matter* 7 (21) (2011) 9804–9828.
- [17] H. Bagheri, M. Aliofkhaezai, H. M. Forooshani, A. S. Rouhaghdam, Electrodeposition of the hierarchical dual structured (hds) nanocrystalline ni surface with high water repellency and self-cleaning properties, *J. Taiwan Inst. Chem. Eng.* 80 (2017) 883–893.
- [18] C.-Y. Lin, K.-Y. A. Lin, T.-W. Yang, Y.-C. Chen, H. Yang, Self-assembled hemispherical nanowell arrays for superhydrophobic antireflection coatings, *J. Colloid Interface Sci.* 490 (2017) 174–180.
- [19] J. Lomga, P. Varshney, D. Nanda, M. Satapathy, S. Mohapatra, A. Kumar, Fabrication of durable and regenerable superhydrophobic coatings with excellent self-cleaning and anti-fogging properties for aluminium surfaces, *J. Alloys Compd* 702 (2017) 161–170.
- [20] Y. Rahmawan, L. Xu, S. Yang, Self-assembly of nanostructures towards transparent, superhydrophobic surfaces, *J. Mater. Chem. A* 1 (9) (2013) 2955–2969.
- [21] M. J. Kreder, J. Alvarenga, P. Kim, J. Aizenberg, Design of anti-icing surfaces: smooth, textured or slippery?, *Nat. Rev. Mater.* 1 (1) (2016) 15003.
- [22] M. A. Sarshar, C. Swartz, S. Hunter, J. Simpson, C.-H. Choi, Effects of contact angle hysteresis on ice adhesion and growth on superhydrophobic surfaces under dynamic flow conditions, *Colloid Polym. Sci.* 291 (2) (2013) 427–435.
- [23] C.-H. Xue, X.-J. Guo, J.-Z. Ma, S.-T. Jia, Fabrication of robust and antifouling superhydrophobic surfaces via surface-initiated atom transfer radical polymerization, *ACS Appl. Mater. Interfaces* 7 (15) (2015) 8251–8259.
- [24] E. Karatay, A. S. Haase, C. W. Visser, C. Sun, D. Lohse, P. A. Tsai, R. G. Lammertink, Control of slippage with tunable bubble mattresses, *PNAS* 110 (21) (2013) 8422–8426.
- [25] J. P. Rothstein, Slip on superhydrophobic surfaces, *Annu. Rev. Fluid Mech.* 42 (2010) 89–109.
- [26] L. Bocquet, E. Lauga, A smooth future?, *Nat. Mater.* 10 (5) (2011) 334.
- [27] P. Tsai, A. M. Peters, C. Pirat, M. Wessling, R. G. Lammertink, D. Lohse, Quantifying effective slip length over micropatterned hydrophobic surfaces, *Physics of Fluids* 21 (11) (2009) 112002.
- [28] D. V. Krishnan, G. U. Kumar, S. Suresh, M. Jubal, M. Thansekhar, R. Ramesh, Wetting transition in laser-fabricated hierarchical surface structures and its impact on condensation heat transfer characteristics, *Int. J. Heat Mass Transf.* 140 (2019) 886–896.
- [29] R. Liu, Z. Liu, Study of boiling heat transfer on concave hemispherical nanostructure surface with md simulation, *Int. J. Heat Mass Transf.* 143 (2019) 118534.
- [30] T. P. Allred, J. A. Weibel, S. V. Garimella, The petal effect of parahydrophobic surfaces offers low receding contact angles that promote effective boiling, *Int. J. Heat Mass Transf.* 135 (2019) 403–412.
- [31] K. S. Boyina, A. J. Mahvi, S. Chavan, D. Park, K. Kumar, M. Lira, Y. Yu, A. A. Gunay, X. Wang, N. Miljkovic, Condensation frosting on meter-scale superhydrophobic and superhydrophilic heat exchangers, *Int. J. Heat Mass Transf.* 145 (2019) 118694.
- [32] D. Quéré, Non-sticking drops, *Reports Prog. Phys.* 68 (11) (2005) 2495.
- [33] A. Cassie, S. Baxter, Wettability of porous surfaces, *J. Chem. Soc. Faraday Trans.* 40 (1944) 546–551.
- [34] T. Koishi, K. Yasuoka, S. Fujikawa, T. Ebisuzaki, X. C. Zeng, Coexistence and transition between cassie and wenzel state on pillared hydrophobic surface, *Proc. Natl. Acad. Sci.* 106 (21) (2009) 8435–8440.
- [35] R. N. Wenzel, Resistance of solid surfaces to wetting by water, *Ind. Eng. Chem.* 28 (8) (1936) 988–994.
- [36] P. Cai, N. Bai, L. Xu, C. Tan, Q. Li, Fabrication of superhydrophobic wood surface with enhanced environmental adaptability through a solution-immersion process, *Surf. Coatings Technol.* 277 (2015) 262–269.
- [37] S. S. Farhadi, M. Aliofkhaezai, G. h. B. Darband, A. Abolhasani, A. S. Rouhaghdam, Corrosion and wettability of peo coatings on magnesium by addition of potassium stearate, *J. Magnes. Alloy.* 5 (2) (2017) 210–216.
- [38] N. Shardt, M. B. Bigdeli, J. A. W. Elliott, P. A. Tsai, How surfactants affect droplet wetting on hydrophobic microstructures, *The Journal of Physical Chemistry Letters* 10 (23) (2019) 7510–7515.
- [39] A. Aldhaleai, P. A. Tsai, Effect of a cationic surfactant on droplet wetting on superhydrophobic surfaces, *Langmuir* 36 (16) (2020) 4308–4316.
- [40] P. Guo, S. Zhai, Z. Xiao, Q. An, One-step fabrication of highly stable, superhydrophobic composites from controllable and low-cost pmhs/teos sols for efficient oil cleanup, *J. Colloid Interface Sci.* 446 (2015) 155–162.
- [41] S. Heinonen, E. Huttunen-Saarivirta, J.-P. Nikkanen, M. Raulio, O. Priha, J. Laakso, E. Storgårds, E. Levänen, Antibacterial properties and chemical stability of superhydrophobic silver-containing surface produced by sol–gel route, *Colloids Surfaces A Physicochem. Eng. Asp.* 453 (2014) 149–161.
- [42] Y. C. Jung, B. Bhushan, Wetting transition of water droplets on superhydrophobic patterned surfaces, *Scr. Mater.* 57 (12) (2007) 1057–1060.
- [43] B. Bhushan, K. Koch, Y. C. Jung, Nanostructures for superhydrophobicity and low adhesion, *Soft Matter* 4 (9) (2008) 1799–1804.
- [44] M. Reyssat, J. Yeomans, D. Quéré, Impalement of fakir drops, *EPL* 81 (2) (2007) 26006.
- [45] P. Tsai, R. G. Lammertink, M. Wessling, D. Lohse, Evaporation-triggered wetting transition for water droplets upon hydrophobic microstructures, *Phys. Rev. Lett.* 104 (11) (2010) 116102.
- [46] W. Xu, R. Leeladhar, Y. T. Kang, C.-H. Choi, Evaporation kinetics of sessile water droplets on micropillared superhydrophobic

- surfaces, *Langmuir* 29 (20) (2013) 6032–6041.
- [47] C. Antonini, J. B. Lee, T. Maitra, S. Irvine, D. Derome, M. K. Tiwari, J. Carmeliet, D. Poulikakos, Unraveling wetting transition through surface textures with x-rays: Liquid meniscus penetration phenomena, *Sci. Rep.* 4 (2014) 4055.
 - [48] J. Lee, S.-H. Hwang, S.-S. Yoon, D.-Y. Khang, Evaporation characteristics of water droplets in cassie, wenzel, and mixed states on superhydrophobic pillared si surface, *Colloids Surfaces A Physicochem. Eng. Asp.* 562 (2019) 304–309.
 - [49] S. Dash, S. V. Garimella, Droplet evaporation dynamics on a superhydrophobic surface with negligible hysteresis, *Langmuir* 29 (34) (2013) 10785–10795.
 - [50] L. Xu, Z. Li, S. Yao, Directional motion of evaporating droplets on gradient surfaces, *Appl. Phys. Lett.* 101 (6) (2012) 064101.
 - [51] G. McHale, S. Aqil, N. Shirtcliffe, M. Newton, H. Y. Erbil, Analysis of droplet evaporation on a superhydrophobic surface, *Langmuir* 21 (24) (2005) 11053–11060.
 - [52] X. Chen, R. Ma, J. Li, C. Hao, W. Guo, B. L. Luk, S. C. Li, S. Yao, Z. Wang, Evaporation of droplets on superhydrophobic surfaces: Surface roughness and small droplet size effects, *Physical review letters* 109 (11) (2012) 116101.
 - [53] F. Wang, H. Wu, Molecular origin of contact line stick-slip motion during droplet evaporation, *Sci. Rep.* 5 (2015) 17521.
 - [54] Á. G. Marín, H. Gelderblom, A. Susarrey-Arce, A. van Houselt, L. Lefferts, J. G. Gardeniers, D. Lohse, J. H. Snoeijer, Building microscopic soccer balls with evaporating colloidal fakir drops, *Proc. Natl. Acad. Sci. U.S.A.* 109 (41) (2012) 16455–16458.
 - [55] R. M. d. Nascimento, C. Cottin-Bizonne, C. Pirat, S. M. Ramos, Water drop evaporation on mushroom-like superhydrophobic surfaces: temperature effects, *Langmuir* 32 (8) (2016) 2005–2009.
 - [56] L. Zhao, C. Hong, L. Lin, H. Wu, Y. Su, X. Zhang, A. Liu, Controllable nanoscale engineering of vertically aligned mos2 ultrathin nanosheets by nitrogen doping of 3d graphene hydrogel for improved electrocatalytic hydrogen evolution, *Carbon N. Y.* 116 (2017) 223–231.
 - [57] C. Dorrer, J. Rühe, Mimicking the stenocara beetle- dewetting of drops from a patterned superhydrophobic surface, *Langmuir* 24 (12) (2008) 6154–6158.
 - [58] V. Kondrashov, J. Rühe, Microcones and nanograss: toward mechanically robust superhydrophobic surfaces, *Langmuir* 30 (15) (2014) 4342–4350.
 - [59] V. Jokinen, L. Sainiemi, S. Franssila, Complex droplets on chemically modified silicon nanograss, *Adv. Mater.* 20 (18) (2008) 3453–3456.
 - [60] C. Dorrer, J. Rühe, Wetting of silicon nanograss: from superhydrophilic to superhydrophobic surfaces, *Adv. Mater.* 20 (1) (2008) 159–163.
 - [61] K. Gjerde, R. R. Kumar, K. N. Andersen, J. Kjelstrup-Hansen, K. B. Teo, W. I. Milne, C. Persson, K. Mølhave, H.-G. Rubahn, P. Bøggild, On the suitability of carbon nanotube forests as non-stick surfaces for nanomanipulation, *Soft Matter* 4 (3) (2008) 392–399.
 - [62] C. A. Schneider, W. S. Rasband, K. W. Eliceiri, Nih image to imagej: 25 years of image analysis, *Nat. Methods* 9 (7) (2012) 671.
 - [63] O. Del Río, A. Neumann, Axisymmetric drop shape analysis: computational methods for the measurement of interfacial properties from the shape and dimensions of pendant and sessile drops, *J. Colloid Interface Sci.* 196 (2) (1997) 136–147.
 - [64] H. A. Wege, J. A. Holgado-Terriza, J. I. Rosales-Leal, R. Osorio, M. Toledano, M. Á. Cabrerizo-Vílchez, Contact angle hysteresis on dentin surfaces measured with adsa on drops and bubbles, *Colloids Surfaces A Physicochem. Eng. Asp.* 206 (1-3) (2002) 469–483.
 - [65] M. Hoorfar, A. Neumann, Axisymmetric drop shape analysis (adsa) for the determination of surface tension and contact angle, *J. Adhes.* 80 (8) (2004) 727–743.
 - [66] H. Gelderblom, A. G. Marin, H. Nair, A. Van Houselt, L. Lefferts, J. H. Snoeijer, D. Lohse, How water droplets evaporate on a superhydrophobic substrate, *Phys. Rev. E* 83 (2) (2011) 026306.
 - [67] S. Kulinich, M. Farzaneh, Effect of contact angle hysteresis on water droplet evaporation from super-hydrophobic surfaces, *Appl. Surf. Sci.* 255 (7) (2009) 4056–4060.
 - [68] M. Lee, W. Kim, S. Lee, S. Baek, K. Yong, S. Jeon, Water droplet evaporation from sticky superhydrophobic surfaces, *Applied Physics Letters* 111 (2) (2017) 021603.
 - [69] R. Picknett, R. Bexon, The evaporation of sessile or pendant drops in still air, *J. Colloid Interface Sci.* 61 (2) (1977) 336–350.
 - [70] Y.-S. Yu, Z. Wang, Y.-P. Zhao, Experimental and theoretical investigations of evaporation of sessile water droplet on hydrophobic surfaces, *J. Colloid Interface Sci.* 365 (1) (2012) 254–259.
 - [71] X. Chen, R. Ma, J. Li, C. Hao, W. Guo, B. L. Luk, S. C. Li, S. Yao, Z. Wang, Evaporation of droplets on superhydrophobic surfaces: Surface roughness and small droplet size effects, *Phys. Rev. Lett.* 109 (11) (2012) 116101.
 - [72] M. R. Gunjan, R. Raj, Dynamic roughness ratio-based framework for modeling mixed mode of droplet evaporation, *Langmuir* 33 (28) (2017) 7191–7201.
 - [73] S. Gao, J. Long, W. Liu, Z. Liu, Evaporation-induced wetting transition of nanodroplets on nanopatterned surfaces with concentric rings: Surface geometry and wettability effects, *Langmuir* 35 (29) (2019) 9546–9553.
 - [74] C. Bourges-Monnier, M. Shanahan, Influence of evaporation on contact angle, *Langmuir* 11 (7) (1995) 2820–2829.
 - [75] J. K. Park, J. Ryu, B. C. Koo, S. Lee, K. H. Kang, How the change of contact angle occurs for an evaporating droplet: effect of impurity and attached water films, *Soft Matter* 8 (47) (2012) 11889–11896.
 - [76] J.-H. Kim, S. I. Ahn, J. H. Kim, W.-C. Zin, Evaporation of water droplets on polymer surfaces, *Langmuir* 23 (11) (2007) 6163–6169.
 - [77] B. Bhushan, M. Nosonovsky, The rose petal effect and the modes of superhydrophobicity, *Phil. Trans. R. Soc. A* 368 (1929) (2010) 4713–4728.
 - [78] Z. Li, Y. Zheng, L. Cui, Preparation of metallic coatings with reversibly switchable wettability based on plasma spraying technology, *J. Coat. Technol. Res.* 9 (5) (2012) 579–587.
 - [79] A. I. Safonov, V. S. Sulyaeva, E. Y. Gatapova, S. V. Starinskiy, N. I. Timoshenko, O. A. Kabov, Deposition features and wettability behavior of fluoropolymer coatings from hexafluoropropylene oxide activated by nicr wire, *Thin Solid Films* 653 (2018) 165–172.
 - [80] M. E. Shanahan, Simple theory of" stick-slip" wetting hysteresis, *Langmuir* 11 (3) (1995) 1041–1043.
 - [81] C. Extrand, A. Gent, Retention of liquid drops by solid surfaces, *Journal of Colloid and Interface Science* 138 (2) (1990) 431–442.
 - [82] C. W. Extrand, Y. Kumagai, Liquid drops on an inclined plane: the relation between contact angles, drop shape, and retentive force, *Journal of colloid and interface science* 170 (2) (1995) 515–521.
 - [83] M. Nosonovsky, Model for solid-liquid and solid-solid friction of rough surfaces with adhesion hysteresis, *J. Chem. Phys.* 126 (22) (2007) 224701.
 - [84] D. Pilat, P. Papadopoulos, D. Schaffel, D. Vollmer, R. Berger, H.-J. Butt, Dynamic measurement of the force required to move a liquid drop on a solid surface, *Langmuir* 28 (49) (2012) 16812–16820.

- [85] E. Bormashenko, A. Musin, G. Whyman, M. Zinigrad, Wet-ting transitions and depinning of the triple line, *Langmuir* 28 (7) (2012) 3460–3464.
- [86] D. Orejon, K. Sefiane, M. E. Shanahan, Stick–slip of evaporat-ing droplets: substrate hydrophobicity and nanoparticle concen-tration, *Langmuir* 27 (21) (2011) 12834–12843.
- [87] M. Shanahan, K. Sefiane, Kinetics of triple line motion during evaporation, *Contact angle, wettability and adhesion* 6 (2009) 19–31.
- [88] S. Ramos, J. Dias, B. Canut, Drop evaporation on superhy-drophobic ptfe surfaces driven by contact line dynamics, *J. Col-loid Interface Sci.* 440 (2015) 133–139.
- [89] Y. O. Popov, Evaporative deposition patterns: spatial dimen-sions of the deposit, *Phys. Rev. E* 71 (3) (2005) 036313.
- [90] T. A. Nguyen, A. V. Nguyen, M. A. Hampton, Z. P. Xu, L. Huang, V. Rudolph, Theoretical and experimental analysis of droplet evaporation on solid surfaces, *Chem. Eng. Sci.* 69 (1) (2012) 522–529.
- [91] S. Dehaeck, A. Rednikov, P. Colinet, Vapor-based interferomet-ric measurement of local evaporation rate and interfacial tem-perature of evaporating droplets, *Langmuir* 30 (8) (2014) 2002–2008.
- [92] F. Carle, B. Sobac, D. Brutin, Experimental evidence of the at-mospheric convective transport contribution to sessile droplet evaporation, *Appl. Phys. Lett.* 102 (6) (2013) 061603.
- [93] S. Dash, S. V. Garimella, Droplet evaporation on heated hy-drophobic and superhydrophobic surfaces, *Phys. Rev. E* 89 (4) (2014) 042402.
- [94] Z. Pan, S. Dash, J. A. Weibel, S. V. Garimella, Assessment of water droplet evaporation mechanisms on hydrophobic and superhydrophobic substrates, *Langmuir* 29 (51) (2013) 15831–15841.
- [95] Z. Pan, J. A. Weibel, S. V. Garimella, Influence of surface wet-tability on transport mechanisms governing water droplet evap-oration, *Langmuir* 30 (32) (2014) 9726–9730.